Three-Dimensional Solution Structure of α-Conotoxin MII, an $\alpha_3\beta_2$ Neuronal Nicotinic Acetylcholine Receptor-Targeted Ligand[†,‡]

Ki-Joon Shon,*[,§] Steven C. Koerber,[||] Jean E. Rivier,[||] Baldomero M. Olivera,[⊥] and J. Michael McIntosh[⊥,#]

Department of Physiology and Biophysics, Case Western Reserve University, Cleveland, Ohio 44106, The Clayton Foundation Laboratories for Peptide Biology, The Salk Institute for Biological Studies, La Jolla, California 92037, and Departments of Biology and Psychiatry, University of Utah, Salt Lake City, Utah 84112

Received June 17, 1997; Revised Manuscript Received September 17, 1997[⊗]

ABSTRACT: α-Conotoxin MII, isolated from *Conus magus*, is a potent peptidic toxin which specifically targets the mammalian neuronal nicotinic acetylcholine receptor, $\alpha_3\beta_2$ subtype. The three-dimensional structure of α-conotoxin MII in aqueous solution has been determined by two-dimensional ^{1}H NMR spectroscopy. NOE-derived distances, refined by an iterative relaxation matrix approach, as well as dihedral and chirality restraints were used in high-temperature biphasic simulated annealing calculations. Fourteen minimum energy structures out of 50 subjected to the SA simulations were chosen for evaluation; these 14 structures have a final RMS deviation of 0.76 ± 0.31 and 1.35 ± 0.34 Å for the backbone and heavy atoms, respectively. The overall structure is unusually well-defined due to a large helical component around the two disulfide bridges. The principal backbone folding motif may be common to a subclass of α-conotoxins. There are two distinct surfaces on the molecule almost at right angles to one another. One entirely consists of the hydrophobic residues Gly[1], Cys[2], Cys[3], Leu[15], and Cys[16]. The second comprises the hydrophilic residues Glu[11], His[12], Ser[13], and Asn[14]. These surfaces on the ligand could be essential for the subtype-specific recognition of the receptor.

Nicotinic acetylcholine receptors (nAChRs)[1] are ligand-gated ion channels which are key components of nervous systems. The classical role for these receptors was defined at the neuromuscular junction: nicotinic receptors concentrated on the muscle end plate serve as the key macromolecules that detect release of neurotransmitter from the presynaptic terminus of the motor axon. However, in addition to these skeletal muscle nicotinic receptors, many other molecular forms of nicotinic receptors exist; these are generally referred to as neuronal nicotinic receptors (nAChRs) (*1*). Their biological roles are much less well understood.

Recently, our laboratories have developed the use of small peptides found in the venom of cone snails to investigate the different molecular forms of nicotinic receptors. One family of *Conus* peptides, the α-conotoxins (CTxs) listed in Table 1, is targeted to the acetylcholine binding site of nicotinic receptors. Typically, the venom from a given species of *Conus* has multiple α-CTxs, some of which are specifically targeted to particular subtypes of neuronal nicotinic receptors. One such peptide is α-CTx MII (*2*).

In order to understand how α-CTxs discriminate between different molecular forms of nicotinic receptors, a structural analysis of α-CTxs that have differential molecular specificity must be carried out. The structure of α-CTx GI, a peptide which at nanomolar concentrations blocks muscle, but not neuronal, nAChRs, has been published (*3*−*5*). Here we report the solution structure of α-CTx MII, a peptide which potently blocks the mammalian $\alpha_3\beta_2$ neuronal nAChR but not the muscle nAChR. Clearly, a comparison between two α-CTx structures that have highly distinct target specificities will contribute to an understanding of how these small peptides can differentially target a particular molecular form of nicotinic receptors.

Structure/activity relationships of α-CTxs that target $\alpha_3\beta_2$ neuronal nicotinic receptors with high specificity may have special biomedical significance. Recently, evidence has been obtained indicating that the $\alpha_3\beta_2$ neuronal nAChR subtype modulates dopamine release at striatal synapses (*6*). Since many psychotic states are alleviated by compounds which inhibit dopaminergic transmission (e.g., drugs effective for schizophrenia), the ability to selectively block the function of the $\alpha_3\beta_2$ nicotinic receptor by specifically targeted nicotinic antagonists may be ultimately useful for designing drugs for clinical use. Thus, structure/function insights into how α-CTx MII selectively binds the $\alpha_3\beta_2$ nicotinic receptor could contribute to the development of novel antipsychotic agents.

[†] This work was supported by NIH Grant GM 54710 and start-up funds from Case Western Reserve University (to K.-J.S.) and by NIH Grants P01 48677 and MH 53631.

[‡] Coordinates of α-conotoxin MII have been deposited in the Brookhaven Protein Data Bank, Upton, NY 11973, under accession code 1m2c.

* To whom all correspondence should be addressed.

[§] Case Western Reserve University.

[||] The Salk Institute for Biological Studies.

[⊥] Department of Biology, University of Utah.

[#] Department of Psychiatry, University of Utah.

[⊗] Abstract published in *Advance ACS Abstracts,* November 15, 1997.

[1] Abbreviations: NMR, nuclear magnetic resonance; NOE, nuclear Overhauser effect; $d_{\alpha N}$, distance between Hα of residue *i* and HN of residue *i*+1; d_{NN}, distance between NH of residue *i* and HN of residue *i*+1; $d_{NN(i,i+2)}$, distance between HN of residue *i* and HN of residue *i*+2; $d_{\alpha N(i,i+2)}$, distance between Hα of residue *i* and HN of residue *i*+2; RMS, root mean square; nAChR, nicotinic acetylcholine receptor; CTx, conotoxin; Fmoc, fluorenylmethyloxycarbonyl; NOESY, NOE spectroscopy; TOCSY, total correlation spectroscopy; DQF-COSY, double quantum filtered correlation spectroscopy; PE-COSY, primitive exclusive correlation spectroscopy; FID, free induction decay; DGII, distance geometry; IRMA, iterative relaxation matrix approach; RMD, restrained molecular dynamics; MD, molecular dynamics; SA, simulated annealing.

S0006-2960(97)01443-8 CCC: $14.00

Table 1: Amino Acid Sequences of α-Conotoxins[a]

α-CTx	Sequence	nAChR	ref
MII	GCCSNPVCHLEHSNLC*	α3β2	2
EI	RDOCCYHPTCNMSNPQIC*	α1β1δγ	47
PnIA	GCCSLPPCAANNPDYC*	molluscan	42
PnIB	GCCSLPPCALSNPDYC*	molluscan	42
GI	ECCNPACGRHYSC*	α1β1δγ	36
GIA	ECCNPACGRHYSCGK*	α1β1δγ	36
GII	ECCHPACGKHFSC*	α1β1δγ	36
MI	GRCCHPACGKNYSC*	α1β1δγ	37,44
SI	ICCNPACGPKYSC*	α1β1δγ	45
SIA	YCCHPACGKNFDC*	α1β1δγ	46
ImI	GCCSDPRCAWRC*	α7,α9	52

[a] Disulfide bonding: CC- - -C- - -C. A single asterisk indicates that the COOH-terminal α-carboxyl group is known to be amidated.

EXPERIMENTAL PROCEDURES

Peptide Synthesis, Folding, and Purification. α-CTx MII, originally isolated from *Conus magus*, was chemically synthesized using standard Fmoc chemistry on an ABI model 431 peptide synthesizer and properly folded to its biologically active conformation using two-step oxidation protocols (*7*). Once purified, the peptide's identity with the native α-CTx MII was confirmed as described in Cartier et al. (*2*).

NMR Spectroscopy. A sample containing 8 mg of the peptide was dissolved in 500 μL of 5 mM sodium phosphate buffer made of 90% H_2O and 10% D_2O (Cambridge Isotope Laboratory). The final pH of the peptide solution was 3.3, and the peptide concentration was 9.4 mM. For experiments requiring "100%" replacement of labile amide hydrogens with deuterons, the sample was lyophilized and dissolved in D_2O (99.96% isotope enriched). After being allowed to sit overnight at room temperature, the sample was again lyophilized and dissolved in D_2O (99.996% isotope enriched).

All NMR data were obtained with a Varian 600 MHz Unity Plus spectrometer equipped with a pulsed-field-gradient (*z*) unit. A set of 2-D ^{1}H NMR experiments were carried out at 275 K: these were NOESY (*8*−*10*) with mixing times of 75, 150, 250, and 350 ms, TOCSY (*11, 12*) with a mixing time of 64 ms, DQF-COSY (*13, 14*), and PE-COSY (*15*). All spectra were recorded in a phase-sensitive mode (*16*) with a spectral width of 6600 Hz and 4K data points except for PE-COSY (8K data points). Eight to 32 scans were signal averaged for each free induction decay (FID) with a relaxation delay of 2 s; each 2-D experiment was completed with 400−512 FIDs. In NOESY experiments, the solvent signal was suppressed by gradient echo combined with the WATERGATE sequence (*17*). A "flip-back" pulse was inserted right after the mixing time to restore the residual magnetization along the *z*-axis (*18*). In TOCSY, a spin lock field of 7.7 kHz necessary for the coherence transfer among scalar-coupled ^{1}H spins was generated with the DIPSI-2 sequence (*19*), and water suppression was obtained using the WATERGATE sequence along with minimum presaturation set at the residual water signal during the relaxation delay. In PE-COSY, water suppression was not needed since the sample was prepared in 100% D_2O. A mixing pulse of 30° was used for PE-COSY, and each FID was recorded with 32 scans to compensate for the sensitivity loss due to the small mixing pulse.

2-D NMR data were transferred to a SGI workstation (Indigo^2) and were processed using Felix 95.0 (MSI, San Diego) except for PE-COSY, which was processed using VNMR 5.10 (Varian). FIDs were apodized with a window function (90° and 135° shifted sine bell) in both dimensions prior to Fourier transformation. Each Fourier transformed FID was baseline corrected by applying a third-order polynomial, and each dimension was referenced to a chemical shift value of 4.76 ppm at the residual water signal.

Generation of Dihedral and Distance Restraints. NOE cross peak volumes were measured from NOESY data with four different mixing times using FELIX 95.0. NOE buildup curves were then fitted with a second-order polynomial, and exact distances were generated for all assigned NOE cross peaks. A distance of 1.8 Å was used as an appropriate reference for nonoverlapping geminal Cβ proton cross peaks, as well as for lower distance bounds. Several volumes of nonoverlapping geminal Cβ proton cross peaks were averaged and used for calibrating measured NOE volumes. A pseudoatom correction of 1 Å (*20*) was added to the upper limits of those NOE cross peaks involving spectroscopically degenerate methyl and methylene protons. As for dihedral restraints, $^3J_{HN-Ha}$ coupling constants were measured from a 1-D ^{1}H spectrum recorded with 32K data points and converted to ϕ dihedral angles centered at −120° (±30°) for $^3J_{HN-Ha} > 8.0$ Hz and −60° (±30°) for $^3J_{HN-Ha} < 5.0$ Hz (*21*). $^3J_{\alpha\beta}$ coupling constants were also measured from PE-COSY recorded from the sample whose amide protons were completely exchanged out with deuterons in "100%" D_2O. The measured $^3J_{\alpha\beta}$ coupling constants derived from those residues with an AMX spin system and with nonoverlapping geminal β protons were used for defining χ_1 dihedral angles in combination with the sequential $d_{HN-H\alpha}$ and $d_{\alpha\beta}$ NOE cross peak intensities (*22, 23*).

Initially 99 interresidue NOE cross peaks with a high level of confidence in their assignments were selected and corrected for those NOE cross peaks containing at least one pseudoatom. Fifteen chirality restraints and 11 ϕ and 5 χ_1 dihedral angles were also included in the restraint file for generating an initial set of 10 structures using the DGII (*24*) module of the InsightII program (MSI, San Diego). All structures generated by the DGII calculations had similar overall backbone folding patterns, and thus the lowest energy structure with the minimum number of NOE violations was chosen and subjected to an iterative relaxation matrix approach (IRMA). This procedure improves the accuracy and precision of interproton NOE-derived distance restraints by evaluating the full relaxation network of spins in a molecule (*25*). At this stage, the total of 158 NOE-derived interproton distances (including intraresidue NOEs with pseudoatom correction) along with 16 dihedral angle and 15 chirality restraints were subjected to IRMA and restrained molecular dynamics (RMD) followed by energy minimization steps. Any distances derived from NOEs containing at least one pseudoatom were not treated by IRMA, and therefore those were not refined by the process. Each cycle of IRMA took experimental NOE intensities measured as a function of mixing time and merged them with the calculated theoretical NOE intensity values for the model structure. A new set of distance restraints was then deduced from this mixed NOE intensity matrix. A rotational correlation time of 1.5 ns, estimated from NOE buildup curves of nonoverlapping geminal β protons, and diagonal leakage rate of 1.0 s were used in each IRMA cycle. After each cycle of IRMA, the structure was subjected to RMD and energy minimization steps using a Lennard-Jones potential with a 12.0 Å cutoff. Five cycles of 1000 steps of RMD of 1.0 fs for a duration

of 5 ps was calculated at 700 K followed by cooling over 5 ps at 500 K and another 5 ps at 300 K. The structure was minimized using 100 steps of steepest descents followed by 1500 steps of conjugated gradient minimization. Four IRMA/RMD cycles were carried out, and the convergence was achieved with the final *R*-factors (a measure of the difference in the theoretical and experimental NOE intensities) reaching 0.407 for R_1 and 0.007 for R_6 (reflects $1/r^6$ relationship between NOE intensity and distance, *r*) (*26*). This IRMA/RMD protocol is well documented in the manual provided by the InsightII software for refining distances converted from experimentally measured NOE cross peaks.

Molecular Modeling. Computer models of α-CTx MII were constructed and manipulated using the InsightII and Discover programs (MSI, San Diego) on a Silicon Graphics workstation. Simulated annealing (SA) computations were conducted on a Cray C-90 supercomputer at the San Diego Supercomputer Center. The consistent valence force field of Hagler and co-workers (*27*) was employed for both the DGII and simulated annealing calculations. An extended molecule with two disulfide bridges was constructed as the triply charged cation with full positive charges on the N-terminal nitrogen and the imidazole side chains of His^9 and His^{12}.

Distance Geometry and Simulated Annealing. A triangle inequality bound smoothing and four-dimensional embedding procedure followed by prospective metrization and majorization with a constant weighting scheme was used for DGII calculations with default settings except for an initial energy of 750 kcal/mol and 20 000 steps of built-in simulated annealing with a step size of 0.3 ps.

In order to develop a more qualitative picture of the conformation(s) of α-CTx MII and to generate three-dimensional structures compatible with the NMR data, a protocol based generally on the principles of simulated annealing as developed by Clore and Gronenborn and co-workers (*28*) was employed. The calculations incorporated two notable departures from previous work. First, the interproton distances were introduced in a biphasic manner during high-temperature molecular dynamics (MD); initially they involved only backbone protons, but then subsequently they involved side chain protons. Second, transition from a quartic to a Lennard-Jones nonbonded potential was achieved in a final dynamics phase concomitant with final maturation of the nonbond energy factor. A total of 50 rounds of SA were conducted in order to sample as large a conformational space as practical given computer processor and disk limitations. A final minimization with a convergence criterion of the largest derivative not exceeding 0.01 kcal mol^{-1} $Å^{-1}$ was conducted.

RESULTS

Resonance Assignments. ^1H resonance assignments of α-CTx MII were carried out using DQF-COSY, TOCSY, and NOESY experiments by combining spin systems of individual amino acids with sequential NOE cross peaks arising from neighboring amino acid residues. Even though complete resonance assignments were easily obtained except for the Cβ protons of Ser^{13} (not observed), the 1-D spectrum of the peptide in the amide proton region had a few resonance overlaps. Starting with the unique residue Val^7, identified on the basis of its spin type, sequential $d_{\alpha N}$ NOE connectivity

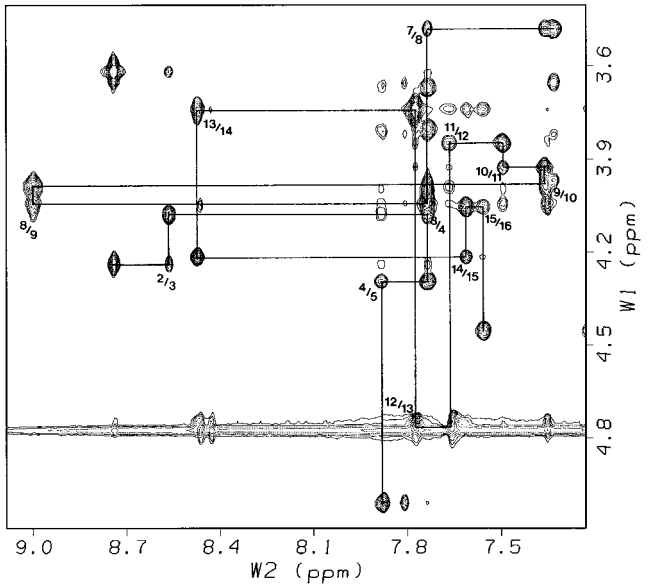

FIGURE 1: NOESY spectrum (250 ms mixing time) of α-CTx MII in H_2O illustrating sequential NOE connectivities between neighboring α and amide protons. The $d_{\alpha N}$ NOE cross peaks are connected by lines and are labeled by residue number. Two traces between residues Cys^2-Asn^5 and Val^7-Cys^{16} are shown with their contiguous connectivities broken at Pro^6.

was traced through the carboxyl terminal residue Cys^{16}. Along the trace, resonance assignment for each residue was confirmed on the basis of its spin type obtained from the TOCSY experiment. The remaining N-terminal residues were also assigned on the basis of sequential $d_{\alpha N}$ NOE connectivity starting from Asn^5, whose spin system was identified from NOE cross peaks between its amide proton and β protons as well as its side chain γ NH_2 protons. In addition, sequential NOEs arising from neighboring amide protons, d_{NN}, confirmed the above resonance assignments. Figure 1 depicts two traces of sequential NOE $d_{\alpha N}$ connectivities which extend from Cys^2 to Asn^5 and from Val^7 to Cys^{16}.

Secondary Structure Determination. It was obvious from both $^3J_{NH-C\alpha}$ coupling constants recorded from a high-resolution 1-D spectrum and short- and medium-range NOE cross peaks from NOESY experiments that a large portion of the peptide was helical. Nine of 16 residues were determined to have $^3J_{NH-C\alpha}$ coupling constants of less than 5.0 Hz, and among those nine residues we have identified short- and medium-range NOE cross peaks, d_{NN}, $d_{NN(i,i+2)}$, $d_{\alpha N}$, and $d_{\alpha N(i,i+2)}$, very typical of an α-helix (*29*). Figure 2 displays those NOE cross peaks according to their intensities along with $^3J_{NH-C\alpha}$ coupling constants used to generate dihedral angle restraints. In addition to the observed NOE cross peaks, Cα proton chemical shifts relative to random-coil values (*29*) are a good assessment for identifying local helical components in peptides and proteins (*30, 31*). The plot shown in Figure 3 strongly suggests that the peptide contains a large portion of helical conformation throughout the sequence except for residues Asn^5 and His^{12}. The backbone conformation of these residues could deviate from a helical conformation on the basis of their positive shifts in the plot.

Structure Calculations and Analysis. A total of 50 structures resulted from the SA calculations described in Experimental Procedures using 154 distance (85 intraresi-

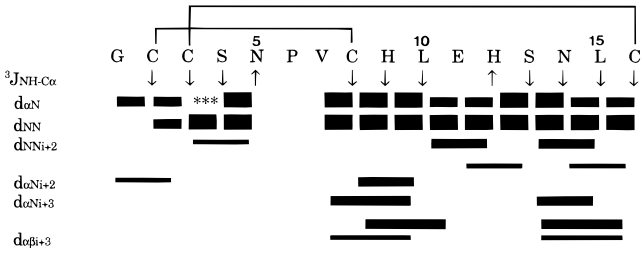

FIGURE 2: Amino acid sequence of α-CTx MII with its disulfide bridges drawn to show its disulfide bridge pattern and a summary of short- to medium-range sequential NOE cross peaks as well as experimentally measured $^3J_{NH-C\alpha H}$ coupling constants. Arrows pointing down are those with ^3J constants <5.0 Hz, and those pointing up are those with ^3J constants >8.0 Hz. Filled bars represent the NOE cross peaks with the thickness classifying NOE intensities from strong (thick) to weak (thin) and the width indicating short- to medium-range separation along the linear sequence. *** represents overlapped NOE cross peaks.

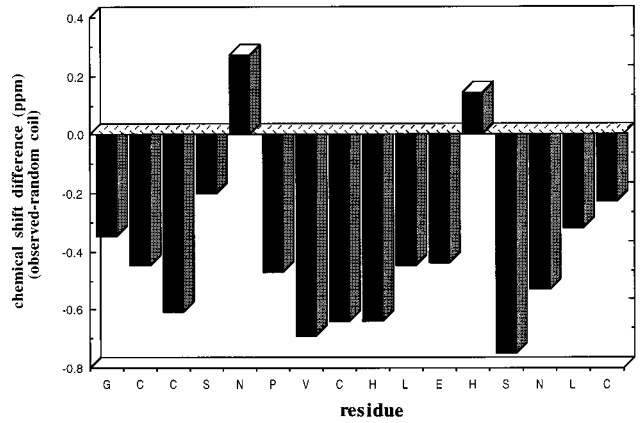

FIGURE 3: α proton chemical shift differences, between observed values from α-CTx MII in H_2O and random-coil values, plotted versus the residue.

due, 42 sequential, 22 medium range, and 5 long range), 14 dihedral, and 15 chirality restraints. An RMS deviation-based family clustering scheme was used which resulted in the grouping of these structures into 30 families spanning the energy range 396−5360 kcal/mol with the two families of lowest energy encompassing 18 of the 50 structures. Structural statistics of these five families, with minimum energy structure (MES) energies within 22 kcal/mol of the overall MES are given in Table 2. The next lowest energy family (family 3) was at 79 kcal/mol relative to the overall MES. By interactive graphical inspection, we have observed that many of the higher energy family representatives (families 3−30) contained unusually high internal energy terms or pathological features (e.g., broken bonds, knots involving backbone and cystine bridges). An interesting structural pathology is observed in structure 8 of family 1 (PDB accession code 1m2c) wherein L-α-Cys[8] is inverted to D-α-Cys[8]. This structure is included because it fits the criterion used for classifying family 1 but in no way influenced the final model and underscores the importance of maintaining proper chirality constraints during SA.

In Figure 4, the structures of family 1 were superimposed to demonstrate how well they converge in the structural calculations with a given set of experimentally determined and refined restraints. As shown in Table 2, the pairwise backbone and heavy atom RMS deviations among those 14 structures in family 1 calculated over residues Cys[2]−Cys[16] (Gly[1] is excluded due to its mobility) are 0.76 ± 0.31 and 1.35 ± 0.34 Å, respectively. In the SA procedure, no particular restraint was employed to force backbone amide bonds to the trans configuration. All amides bonds in all residues of all structures in this family are trans, and all 14 structures in family 1 have almost the same backbone dihedral angles with the exception of Gly[1], as seen from high values of the backbone angular order parameters (*32*, *33*) in Figure 5A,B. However, this consistency of the backbone dihedral angles is not maintained at the level of the χ_1 side chain dihedral. High angular order parameters as seen in Figure 5C for residues 2, 5, 9, and 10 indicate that all structures of family 1 have equivalent side chain rotameric states. All other residues have multiple side chain rotameric states which generally fall into the *gauche*$^-$, *gauche*$^+$, or *trans* classification. The structures of family 1 are well built as judged by the range and magnitude of the energetic contributions detailed in Table 2. Clearly, important energetic contributions to the maintenance of these structures are found in the nonbonded terms, both van der Waals and Coulombic. These modeling studies were conducted *in vacuo*, and any modulation of the effective dielectric constant by either empirical solvation methods or explicit solvent inclusion should serve only to decrease the net effect of electrostatics for this simple constrained peptide.

Table 2: Structural Statistics for the Two Lowest Energy Families of MII Resulting from SA

family	1	2
no. of structures	14	4
energy components[a]		
E_{total}	453 ± 30	476 ± 48
E_{bond}	28 ± 2	28 ± 1
E_{angle}	161 ± 12	165 ± 14
$E_{torsion}$	50 ± 6	63 ± 14
$E_{out\ of\ plane}$	4 ± 1	4 ± 1
$E_{van\ der\ Waals}$	75 ± 8	84 ± 17
$E_{Coulomb}$	135 ± 9	132 ± 9
E_{force}	75 ± 20	77 ± 21
$E_{total+force}$	527 ± 47	553 ± 68
pairwise RMS[b]		
backbone (2−16)	0.76 ± 0.31	0.99 ± 0.25
heavy atoms (2−16)	1.35 ± 0.34	1.61 ± 0.25
NMR violatons >0.2 Å[b]		
av no. of violations per structure	16.64 ± 3.13	16.50 ±3.64
av violation	0.30 ± 0.11	0.31 ± 0.11
dihedral violations >10°	1/14[c] (Cys^2 χ_1)	1/4[d] (Cys^2 χ_1) 2/4[d] (His^9 χ_1)
minimum energy structure		
E_{total}	396	418
$E_{total+force}$	440	463
no. of violations >0.2 Å	13	21
av violation >0.2 Å[b]	0.25 ± 0.04	0.32 ± 0.12
max violation[b]	0.35	0.66

[a] All energies in kcal/mol. [b] All distance in Å. [c] Number of structures in family 1. [d] Number of structures in family 2.

Description of the Structure. Even though α-CTx MII is a small peptide made of only 16 amino acid residues, it has a well-defined three-dimensional solution structure. In addition to two disulfide bridges which form a hydrophobic Cys knot, there are three helical regions in the structure which contribute to form a very tight conformation. The presence of such stable secondary structures and disulfide bridges allows the multidimensional NMR method to be effective in obtaining a very high resolution structure of the peptide. The amino-terminal region has almost a full turn of α-helix (Cys[2]−Ser[4]); this is followed by Asn[5] which has backbone dihedral angles of $\phi = -89°$ and $\psi = +132°$ (measured

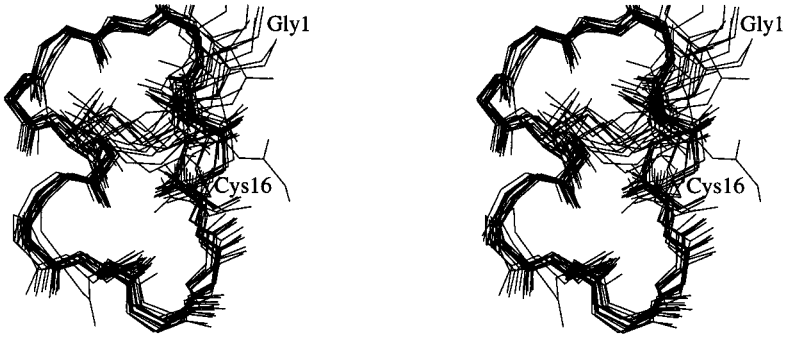

FIGURE 4: Superimposition of the 14 lowest energy structures of α-CTx MII calculated from simulated annealing. Backbone and Cys side chain atoms are illustrated in stereoview.

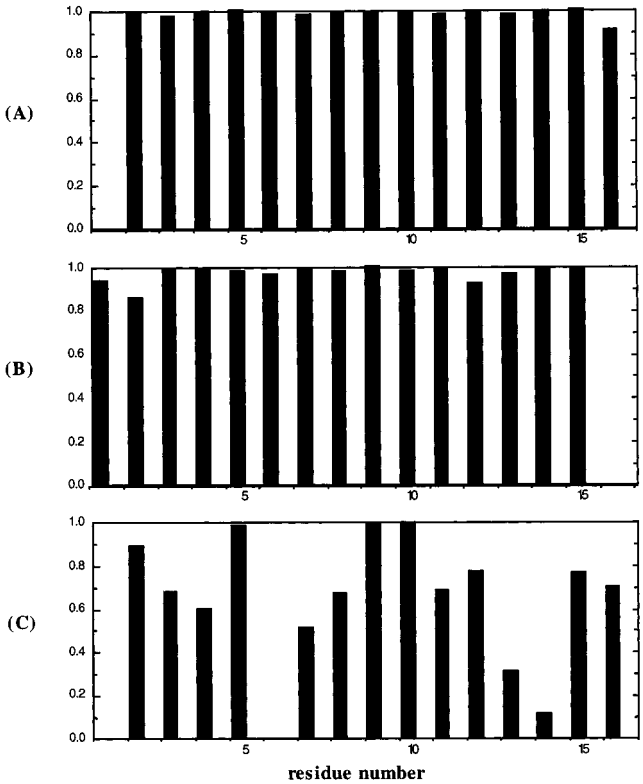

FIGURE 5: Angular order parameters for the backbone ϕ (A), ψ (B), and χ_1 (C) obtained from the 14 minimum energy structures, plotted versus the residue number.

from the minimum energy structure), thereby essentially making a 90° turn. The helix with almost two turns (Pro^6−Glu^{11}) is the major secondary structural component of the peptide. This helix is terminated by His^{12} ($\phi = -136°$, $\psi = +77°$; measured from the minimum energy structure) which orients the remaining C-terminal distorted 3_{10} helix (Ser^{13}−Cys^{16}) toward the N-terminus. These two turns associated with Asn^5 and His^{12} are perhaps critical residues for the overall fold of the peptide, and the presence of such turns is further supported by Cα proton shift data presented in Figure 3 (positive shifts compare to the rest having negative shifts) as well as $^3J_{HN-C\alpha}$ coupling constants in Figure 2 (>8.0 Hz coupling constants compare to the rest having <5.0 Hz). A possible function of Asn^5 is to induce a turn between the N-terminal segment and the main α-helix; this function is consistent with the survey by Richardson and Richardson (*34*) of 215 α-helices from 45 different globular protein structures. They reported a striking preference of 3.5:1 for Asn at the N-cap position and 2.6:1 for Pro at the N-cap + 1 position (helix initiator) for α-helices. With respect to the second turn around His^{12}, the function of His may be to bring Cys^3 and Cys^{16} close together to form the second disulfide bridge.

The space-filling model of α-CTx MII shown in Figure 6B is oriented to explore the surface distribution of hydrophobic and hydrophilic side chain groups of the molecule. Hydrophobic residues are colored purple to distinguish them from polar residues, which are yellow, or charged residues, which are red (positive) and blue (negative). A flat surface located on top of the molecule in purple is a distinct structural feature representing the cluster of hydrophobic residues exposed to solvent. This hydrophobic surface is formed largely by Gly^1 (excluding the N-terminal amino group), Cys^2, Cys^3, Leu^{15}, Cys^{16}, and the disulfide bond between Cys^3 and Cys^{16}. This flat surface may be important for ligand−receptor binding through hydrophobic interactions. There is another very distinct surface that consists entirely of hydrophilic residues with both polar and charged groups. On the left side of the model, the cluster of red, blue, and yellow represents a region of the turn at His^{12} (Glu^{11}−Asn^{14}). This highly charged surface, almost perpendicular to the hydrophobic surface, could be responsible for its initial recognition by nAChR based on long-range electrostatic attractions. This potential receptor-binding interface is composed of sequential residues Glu^{11}, His^{12}, Ser^{13}, and Asn^{14}.

DISCUSSION

In this work, the structure of α-CTx MII has been determined using multidimensional NMR techniques. A comparison of the effects of α-CTx MII on different molecular forms of nAChRs expressed exogenously in *Xenopus* oocytes demonstrated that α-CTx MII has subnanomolar affinity for the $\alpha_3\beta_2$ subtype; in contrast, for all other nAChRs tested the IC_{50} is 2−4 orders of magnitude higher (*2*). Thus, α-CTx MII is the first small peptide known to have high affinity and selectivity for the $\alpha_3\beta_2$ nAChR subtype. The ability to discriminate between diverse molecular forms of nAChRs has considerable significance both for basic neuroscience and for potential drug development. Indeed, the peptide has already been useful for two significant investigations: it was demonstrated that α-CTX MII blocks some (presumably $\alpha_3\beta_2$ mediated) but not all of the nicotinic-evoked dopamine release (*6*). In addition, in one of the well-studied model systems for cholinergic−synaptic transmission, the chick ciliary ganglion, it has recently been demonstrated that there are at least two nAChR subtypes involved. One subtype is blocked by α-CTX MII (putatively $\alpha_3\beta_2$), and the other is blocked by α-bungarotoxin (presumably α_7) (*35*).

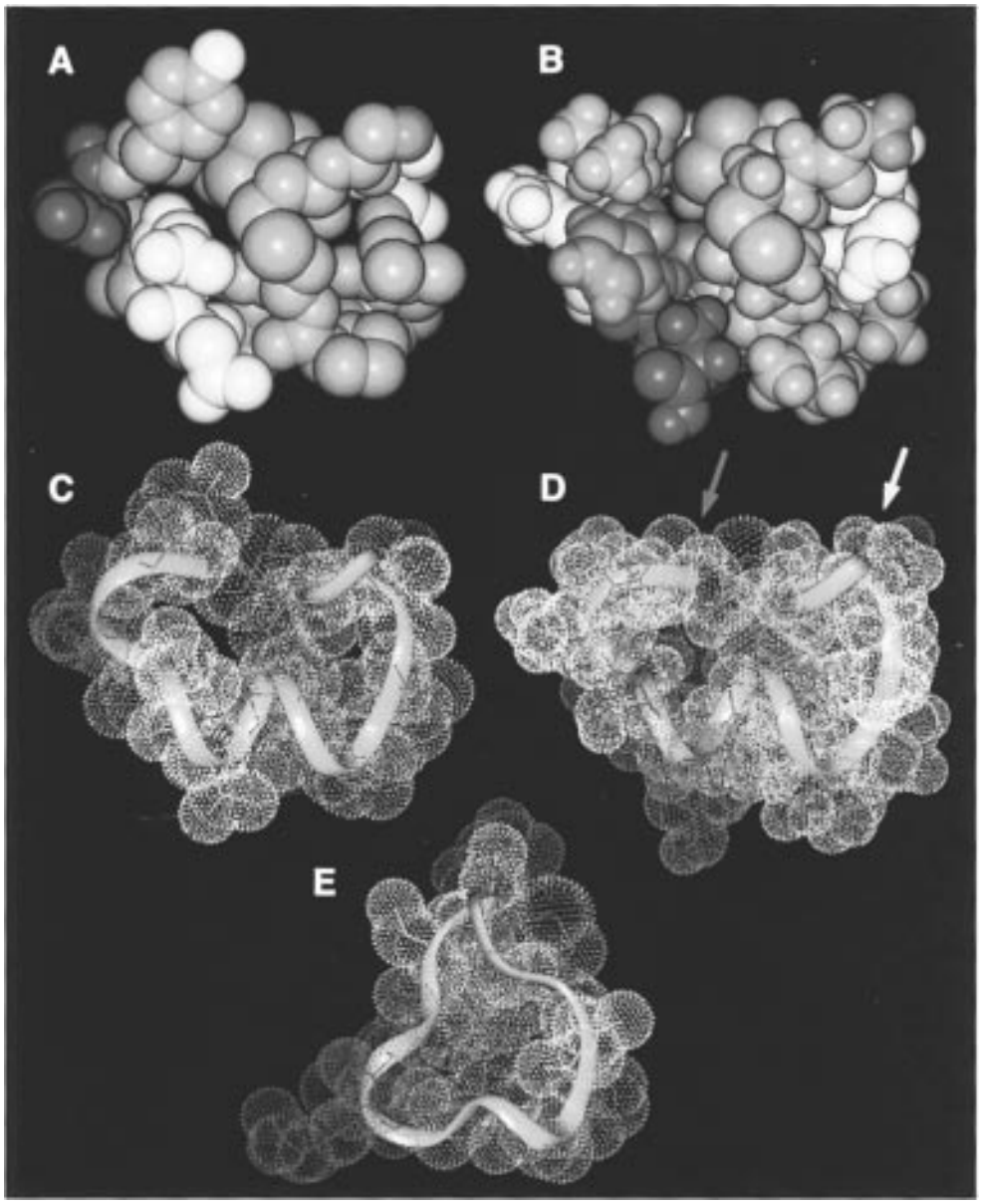

FIGURE 6: Surface (A, B) and backbone (C, D, E) representations of α-CTxs MII, PnIA, and GI. Space-filling models of the X-ray crystal structure of α-CTx PnIA (A) and the lowest energy structure of α-CTx MII (B) are displayed in purple for hydrophobic residues, in yellow for polar side chains, and in red (positive) and blue (negative) for charged side chains. Backbone conformations of α-CTx PnIA (C), α-CTx MII (D), and α-CTx GI (E) are displayed in ribbons and surface distributions in dots with the same color codes to illustrate their similarity and difference. Arrows indicate terminal residues, blue for carboxyl and yellow for amino.

Thus α-CTx MII can distinguish between physiologically linked but structurally distinct nAChR subtypes *in vivo*.

A basic structural question that needs to be addressed is how small peptides belonging to the α-CTx family (which are widely distributed in *Conus* venoms) target a particular molecular form of nAChR. α-CTx GI, the first α-CTx to be discovered (*36*), specifically targets the $\alpha_1\delta$ interface of the mammalian skeletal muscle subtype of nicotinic receptor. α-CTx GI and other related α-CTxs paralytic in vertebrates [including α-CTx MI (*37*) from *C. magus*, the same snail which produces α-CTx MII] are the only known ligands to discriminate between the two ligand-binding sites on the muscle nAChR by several orders of magnitude (*38*−*41*). The structure of α-CTx GI has been solved by both X-ray and NMR methods (*3*−*5*). The specificity of α-CTx MII is entirely different from that of GI, targeting instead the interface between α_3 and β_2 neuronal subunits. Thus, with the elucidation of the structure of α-CTx MII reported here, the structures of two members of the α-CTx family which target well-defined but completely different sites on mammalian nAChRs have now been solved.

The structure of α-CTx MII described above has several striking features that are different from the α-CTx GI structure. There is a clear α-helical segment between Asn^5 and His^{12} in α-CTx MII which is not present in α-GI; instead, the homologous region around the third cysteine residue in the latter peptide is not α-helical, although it has been suggested that it may be a 3_{10} helix. It is notable that the helix N-cap sequence Asn^5 followed by Pro^6 is present in both peptides. The presence of the α-helical region in α-CTx MII not only was consistent with the NOEs obtained but, as discussed above, could also be verified by the α proton shift data shown in Figure 3. This showed the expected negative shift consistent with an α-helical region.

The structure of α-CTx MII has features that are much closer to those of the recently solved structure of α-CTx PnIA

(a peptide reported to selectively target molluscan nAChRs) (*42*, *43*) than those of α-CTx GI (see Figure 6E). As shown in Figure 6, the backbone structures of α-CTx MII and α-CTx PnIA are virtually superimposable. These results suggest that spacing between disulfide bonds may be an important determinant of backbone structure. In α-CTX GI and other related peptides such as α-CTXs MI (*44*), SI (*45*), SIA (*46*), there are three amino acids between the first pair of Cys residues and the third Cys and five amino acids between the third and fourth Cys residues (a configuration called the $\alpha_{3/5}$ pattern). In contrast, the spacing for both α-CTxs MII and PnIA fits an $\alpha_{4/7}$ pattern (see Table 1). There may be fundamental differences between the secondary structure found on the backbone chain of $\alpha_{3/5}$ versus $\alpha_{4/7}$ CTxs. Although α-CTx PnIA has been shown to inhibit nicotinic receptors in molluscan systems, there has been no published molecular definition of any of the high-affinity target sites for α-CTx PnIA. The similarity of the backbone structures of α-CTx MII and α-CTx PnIA might be an evolutionary consequence of their targeting closely related neuronal subtypes rather than the skeletal muscle subtype (which is targeted by α-CTx GI); the large structural differences between α-CTxs MII and GI would therefore be a consequence of evolutionary pressure for selection for two divergent classes of receptor targets. In this regard, it will be of great interest to examine an α-CTx that has the spacing between cysteine residues found for α-CTxs MII and PnIA but which targets the skeletal muscle subtype of nAChR. Indeed, several such peptides have recently been discovered including α-CTx EI (*47*), the structural analysis of which is currently underway.

A comparison of the structures of α-CTxs MII and PnIA is instructive. The two structures are compared in two different ways in Figure 6: panels A and B emphasize the surface features of the two peptides, while panels C and D emphasize the backbone structure. It is clear from the figure that although the backbone structures are strikingly homologous, when the two peptides are viewed using a space-filling model, they look very different from each other. The very flat hydrophobic surface of α-CTx MII contrasts starkly with the tyrosine residue jutting out from α-CTx PnIA. Furthermore, the distribution of charged residues is quite different, with positive and negative charges prominently exposed on the surface of α-CTx MII but not α-CTx PnIA. A similar situation has been found for the *ω*-CTxs which target calcium channels; the backbone structures of *ω*-CTxs GVIA and MVIIC are strikingly similar (*33*, *48*−*50*). However, these two peptides do in fact have different subtype specificities. In contrast, with α-CTxs GI and MII, their backbone structure, surface features, and receptor target specificity all diverge significantly.

The solution structure of α-CTx MII also allows specific predictions to be made concerning which residues are surface exposed and which are buried internally (Cys^8 and His^9) within the peptide. As more structure/function information is collected for α-CTx MII by mutagenesis of both the peptide and the nicotinic receptor, the solution structure that has been elucidated should reveal whether or not any conformational changes take place upon binding of the peptide to its target $\alpha_3\beta_2$ site in the receptor. By making appropriate substitutions in the α-CTx MII structure, accompanied by a parallel mutational study in the receptor (which in fact has already been initiated) (*51*), it should be possible to make pairwise assignments of which residues in the peptide interact with which specific residues in the receptor. For example, if unfolding of the α-helical region of α-CTx MII occurs upon binding to the receptor, then some buried residues would be involved in pairwise interactions in the receptor. However, if no conformational changes took place upon binding, all of the key interacting residues on the peptide that would be identified by a mutational analysis should be surface residues in the structure described here. Thus, the solution structure which has been solved is expected to provide key structural information for interpreting data from experiments examining the interaction of analogs of the toxin with appropriate mutants of the $\alpha_3\beta_2$ nAChR.

ACKNOWLEDGMENT

The following people are greatly appreciated for their help in peptide synthesis (Dr. Robert Schackmann of the Utah Regional Cancer Center), peptide folding and purification (Rick Jacobsen), generating the color figure (G. Edward Cartier and Zoya Maslak), and implementation of multidimensional pulse sequences to NMR spectrometers at the CCSB (Cleveland Center for Structural Biology) (Dr. Frank D. Sonnichsen). We thank Drs. William R. Gray and Doju Yoshikami for their critical reading of the manuscript.

SUPPORTING INFORMATION AVAILABLE

^{1}H resonance assignments of α-CTx MII and its NMR restraint file for the SA calculations (5 pages). Ordering information is given on any current masthead page.

REFERENCES

1. Sargent, P. B. (1993) *Annu. Rev. Neurosci. 16*, 403−443.
2. Cartier, G. E., Yoshikami, D., Gray, W. R., Luo, S., Olivera, B. M., & McIntosh, J. M. (1996) *J. Biol. Chem. 271*, 7522−7528.
3. Pardi, A., Galdes, A., Florance, J., and Maniconte, D. (1989) *Biochemistry 28*, 5494−5501.
4. Kobayashi, Y., Ohkubo, T., Kygoaku, Y., Nishiuchi, Y., Sakakibara, S., Braun, W., and Gö, N. (1989) *Biochemistry 28*, 4853−4860.
5. Guddat, L. W., Martin, J. A., Shan, L., Edmundson, A. B., and Gray, W. R. (1996) *Biochemistry 35*, 11329−11335.
6. Kulak, J. M., Nguyen, T. A., Olivera, B. M., and McIntosh, J. M. (1997) *J. Neurosci. 17*, 5263−5270.
7. Monje, V. D., Haack, J., Naisbitt, S., Miljanich, G., Ramachandran, J., Nasdasdi, L., Olivera, B. M., Hillyard, D. R., and Gray, W. R. (1993) *Neuropharmacology 32*, 1141−1149.
8. Jeener, J., Meier, B. H., Bachmann, P., and Ernst, R. R. (1979) *J. Chem. Phys. 71*, 4546−4553.
9. Kumar, A., Ernst, R. R., and Wuthrich, K. (1980) *Biochem. Biophys. Res. Commun. 95*, 1−6.
10. Macura, S., Huong, Y., Suter, D., and Ernst, R. R. (1981) *J. Magn. Reson. 43*, 259−281.
11. Braunschweiler, L., & Ernst, R. R. (1983) *J. Magn. Reson. 53*, 521−528.
12. Davis, D. G., & Bax, A. (1985) *J. Am. Chem. Soc. 107*, 2820−2821.
13. Piantini, U., Sorensen, O. W., and Ernst, R. R. (1982) *J. Am. Chem. Soc. 104*, 6800−6801.
14. Rance, M., Sorensen, O. W., Bodenhausen, G., Wagner, G., Ernst, R. R., and Wuthrich, K. (1983) *Biochem. Biophys. Res. Commun. 117*, 479−485.
15. Muller, L. (1987) *J. Magn. Reson. 72*, 191−196.
16. States, D. J., Haberkorn, R. A., and Ruben, D. J. (1982) *J. Magn. Reson. 48*, 286−292.
17. Piotto, M., Saudek, V., and Sklenar, V. (1992) *J. Biomol. NMR 2*, 661−665.

18. Tegenfeldt, J., and Haeberlen, U. (1979) *J. Magn. Reson. 36*, 453−457.
19. Rucker, S., and Shaka, A. (1989) *Mol. Phys. 68*, 509−517.
20. Wuthrich, K., Billeter, M., and Braun, W. (1983) *J. Mol. Biol. 169*, 949−961.
21. Pardi, A., Billeter, M., and Wuthrich, K. (1984) *J. Mol. Biol. 180*, 741−751.
22. Hyberts, S., Marki, W., and Wagner, G. (1987) *Eur. J. Biochem. 164*, 625−635.
23. Wagner, G., Braun, W., Havel, T., Schaumann, T., Go, N., and Wuthrich, K. (1987) *J. Mol. Biol. 196*, 611−639.
24. Havel, T. (1991) *Prog. Mol. Biol. Biophys. 56*, 43−78.
25. Boelens, R., Koning, T., & Kaptein, R. (1988) *Mol. Struct. 173*, 299.
26. Gonzales, C., Rullmann, J., Bonvin, A., Boelens, R., and Kaptein, R. (1991) *J. Magn. Reson. 91*, 659−664.
27. Dauber-Osguthorpe, P., Roberts, V., Osguthorpe, D., Wolf, J., Genest, M., and Hagler, A. (1988) *Proteins 4*, 31−47.
28. Nilges, M., Clore, G., and Gronenborn, A. (1988) *FEBS Lett. 239*, 129−136.
29. Wuthrich, K. (1986) *NMR of Proteins and Nucleic Acids*, Wiley-Interscience, New York.
30. Wishart, D. S., Sykes, B. D., and Richards, F. M. (1991) *J. Mol. Biol. 222*, 311−333.
31. Rothemund, S., Krause, E., Beyermann, M., Bienert, M., Sykes, B. D., and Sonnichsen, F. D. (1996) *Biopolymers 39*, 207−219.
32. Hyberts, S., Goldberg, M., Havel, T., and Wagner, G. (1992) *Protein Sci. 1*, 736−751.
33. Pallaghy, P., Duggan, B., Pennington, M., and Norton, R. (1993) *J. Mol. Biol. 234*, 405−420.
34. Richardson, J. S., and Richardson, D. C. (1988) *Science 240*, 1648−1652.
35. Ullian, E. M., McIntosh, J. M., and Sargent, P. B. (1997) *J. Neurosci. 17*, 7210−7219.
36. Gray, W. R., Luque, A., Olivera, B. M., Barrett, J., and Cruz, L. J. (1981) *J. Biol. Chem. 256*, 4734−4740.
37. McIntosh, J. M., Cruz, L. J., Hunkapiller, M. W., Gray, W. R., and Olivera, B. M. (1982) *Arch. Biochem. Biophys. 218*, 329−334.
38. Kreienkamp, H.-J., Sine, S. M., Maeda, R. K., and Taylor, P. (1994) *J. Biol. Chem. 269*, 8108−8114.
39. Hann, R. M., Pagán, O. R., and Eterovic, V. A. (1994) *Biochemistry 33*, 14058−14063.
40. Utkin, Y. N., Kobayashi, F. H., and Tsetlin, V. I. (1994) *Toxicon 32*, 1153−1157.
41. Sine, S. M., Kreienkamp, H.-J., Bren, N., Maeda, R., and Taylor, P. (1995) *Neuron 15*, 205−211.
42. Fainzilber, M., Hasson, A., Oren, R., Burlingame, A. L., Gordon, D., Spira, M. E., and Zlotkin, E. (1994) *Biochemistry 33*, 9523−9529.
43. Hu, S.-H., Gehrmann, J., Guddat, L. W., Alewood, P. F., Craik, D. J., and Martin, J. L. (1996) *Structure 4*, 417−423.
44. Gray, W. R., Rivier, J. E., Galyean, R., Cruz, L. J., and Olivera, B. M. (1983) *J. Biol. Chem. 258*, 12247−12251.
45. Zafaralla, G. C., Ramilo, C., Gray, W. R., Karlstrom, R., Olivera, B. M., and Cruz, L. J. (1988) *Biochemistry 27*, 7102−7105.
46. Myers, R. A., Zafaralla, G. C., Gray, W. R., Abbott, J., Cruz, L. J., and Olivera, B. M. (1991) *Biochemistry 30*, 9370−9377.
47. Martinez, J. S., Olivera, B. M., Gray, W. R., Craig, A. G., Groebe, D. R., Abramson, S. N., and McIntosh, J. M. (1995) *Biochemistry 34*, 14519−14526.
48. Skalicky, J., Metzler, W., Ciesla, D., Galdes, A., and Pardi, A. (1993) *Protein Sci. 2*, 1591−1603.
49. Davis, J., Bradley, E., Miljanich, G., Nadasdi, L., Ramachandran, J., & Basus, V. (1993) *Biochemistry 32*, 7396−7405.
50. Kohno, T., Kim, J., Kobayashi, K., Kodera, Y., Maeda, T., and Sato, K. (1995) *Biochemistry 34*, 10256−10265.
51. Harvey, S. C., McIntosh, J. M., Cartier, G. E., Maddox, F. N., and Luetje, C. W. (1997) *Mol. Pharmacol. 51*, 336−342.
52. McIntosh, J. M., Yoshikami, D., Mahe, E., Nielsen, D. B., Rivier, J. E., Gray, W. R., and Olivera, B. M. (1994) *J. Biol. Chem. 269*, 16733−16739.

BI971443R